Mechanical Reliability of Fullerene/Tin Oxide Interfaces in Monolithic Perovskite/Silicon Tandem Cells

ACS Energy LETTERS

http://pubs.acs.org/journal/aelccp

LETTER

Mechanical Reliability of Fullerene/Tin Oxide Interfaces in Monolithic Perovskite/Silicon Tandem Cells

Michele De Bastiani,* Giovanni Armaroli, Rawan Jalmood, Laura Ferlauto, Xiaole Li, Ran Tao, George T. Harrison, Mathan K. Eswaran, Randi Azmi, Maxime Babics, Anand S. Subbiah, Erkan Aydin, Thomas G. Allen, Craig Combe, Tobias Cramer, Derya Baran, Udo Schwingenschlögl, Gilles Lubineau, Daniela Cavalcoli, and Stefaan De Wolf*

Cite This: https://doi.org/10.1021/acsenergylett.1c02148 Read Online

ACCESS | Metrics & More | Article Recommendations | Supporting Information

ABSTRACT: High-efficiency perovskite-based solar cells comprise sophisticated stacks of materials which, however, often feature different thermal expansion coefficients and are only weakly bonded at their interfaces. This may raise concerns over delamination in such devices, jeopardizing their long-term stability and commercial viability. Here, we investigate the root causes of catastrophic top-contact delamination we observed in state-of-the-art *p-i-n* perovskite/silicon tandem solar cells. By combining macroscopic and microscopic analyses, we identify the interface between the fullerene electron transport layer and the tin oxide buffer layer at the origin of such delamination. Specifically, we find that the perovskite morphology and its roughness play a significant role in the microscopic adhesion of the top layers, as well as the film processing conditions, particularly the deposition temperature and the sputtering power. Our findings mandate the search for new interfacial linking strategies to enable mechanically strong perovskite-based solar cells, as required for commercialization.

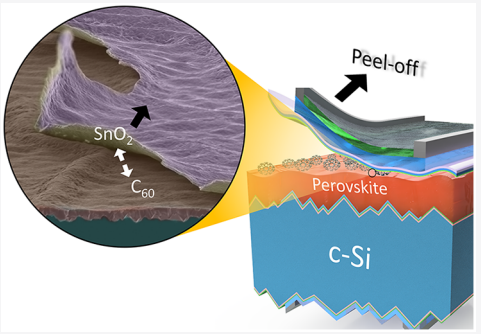

In the past few years, monolithic perovskite/silicon tandems, combining perovskite and silicon solar cell technologies, have enabled high power conversion efficiencies (PCEs) in a possible cost-effective way, which holds great promise for their mass production.[1−3] To date, most of the tandem research has focused on pursuing PCE increases,[4−9] often by introducing sophisticated stacks of materials. However, for commercialization, tandems need to be integrated into solar panels, which may pose significant cell-to-module related technological challenges,[10] which urgently need to be identified and mitigated. Conventional monofacial single-junction crystalline silicon (c-Si) photovoltaic (PV) modules consist of a front glass sheet, strings of series-connected c-Si solar cells, sandwiched between two encapsulant layers (front and rear, at present usually made from ethylene vinyl acetate, EVA), and a polymeric backsheet.[10,11] This stack is then laminated by vacuum annealing to melt and solidify the encapsulant layers, which also aids in anchoring the strings of cells in the module. For module integration of perovskite/silicon tandem solar cells, this process should be altered. Indeed, due to the sensitivity of perovskites to moisture,[12] the backsheet needs to be replaced with a rear glass sheet, acting as a more effective barrier; such glass/glass module technology is already well established for bifacial c-Si PV technology.[11] Moreover, classic module lamination tends to shrink the encapsulant layers upon solidification, which can be several centimeters over the module dimensions. We find this often to cause tandem-device delamination, resulting in catastrophic module failure. For lab-scale devices, this can be resolved by removing the encapsulant layers and sealing the glass/glass modules only at their edges, for instance with butyl-rubber derivatives.[13−15] However, for larger modules, the absence of encapsulants may compromise the anchoring and structural stability of the strings of fragile cells. Therefore, understanding and resolving tandem delamination is a key challenge toward its commercialization.[16] In 2018, Cheacharoen et al. reported on delamination of single-junction perovskite solar cells

Received: October 3, 2021
Accepted: December 30, 2021

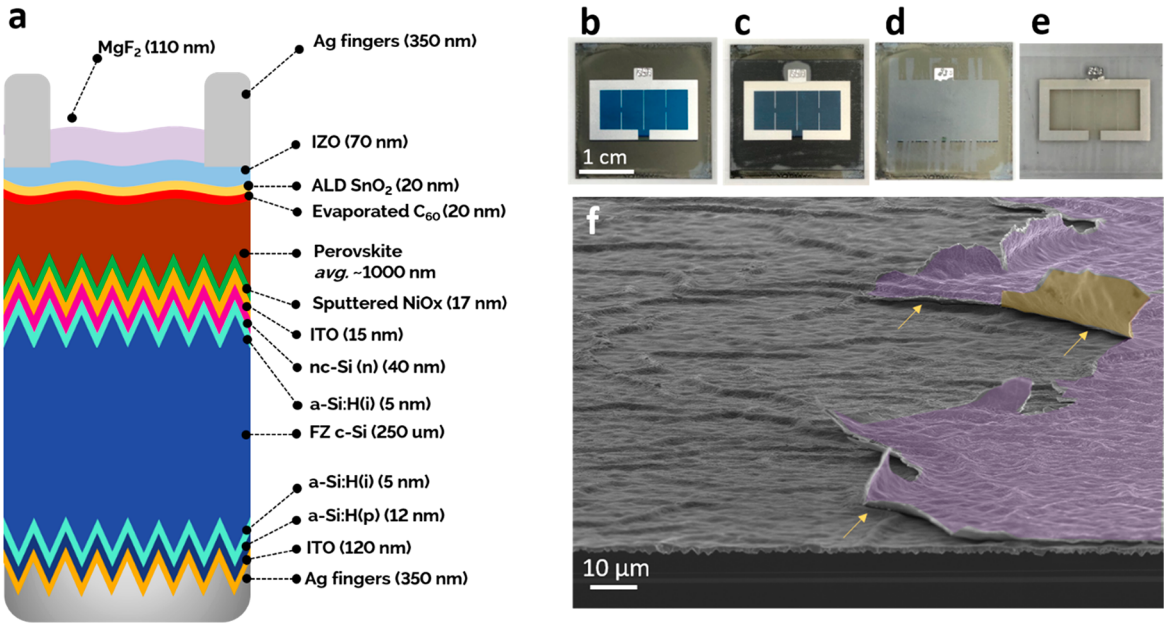

Figure 1. Delamination of the top electrode: (a) structure of the *p-i-n* tandem. (b) Picture of the tandem solar cell, (c) covered by tape, (d) after the peeling, with the emerging surface, and (e) peeled part left on the tape. (f) False-colored tilted SEM image of the peeled electrode. The peeled surface presents the typical wrinkles of the perovskite surface. The purple area represents the top of the Ag/MgF_2 electrode, while the yellow area the lift-off film that delaminated. The yellow arrows indicate the interface where delamination happens.

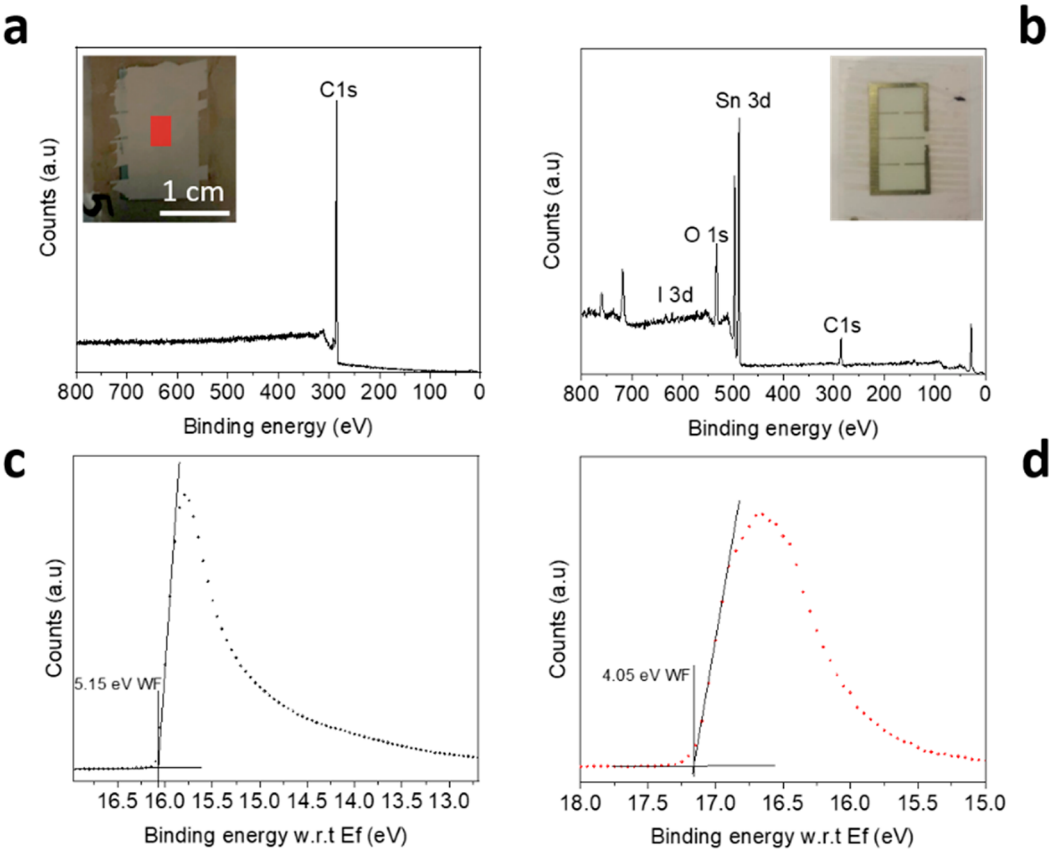

Figure 2. XPS survey of the peeled electrode. (a) XPS survey of the emerging surface. The inset is a picture of the delaminated sample. The red square represents the XPS probed area. (b) XPS survey of the peeled electrode. The inset represents the peeled electrode. (c) UPS spectrum of the emerging surface. (d) UPS spectrum of the peeled electrode.

(PSCs) in the *p-i-n* architecture, the same configuration as most efficient perovskite/silicon tandems.[13,14] With double cantilever beam experiments, they found that the delamination occurs within the electron-selective contact, particularly in the phenyl-C61-butyric acid methyl ester (PCBM) film. This film features the lowest fracture energy among the whole device

https://doi.org/10.1021/acsenergylett.1c02148
ACS Energy Lett. XXXX, XXX, XXX−XXX

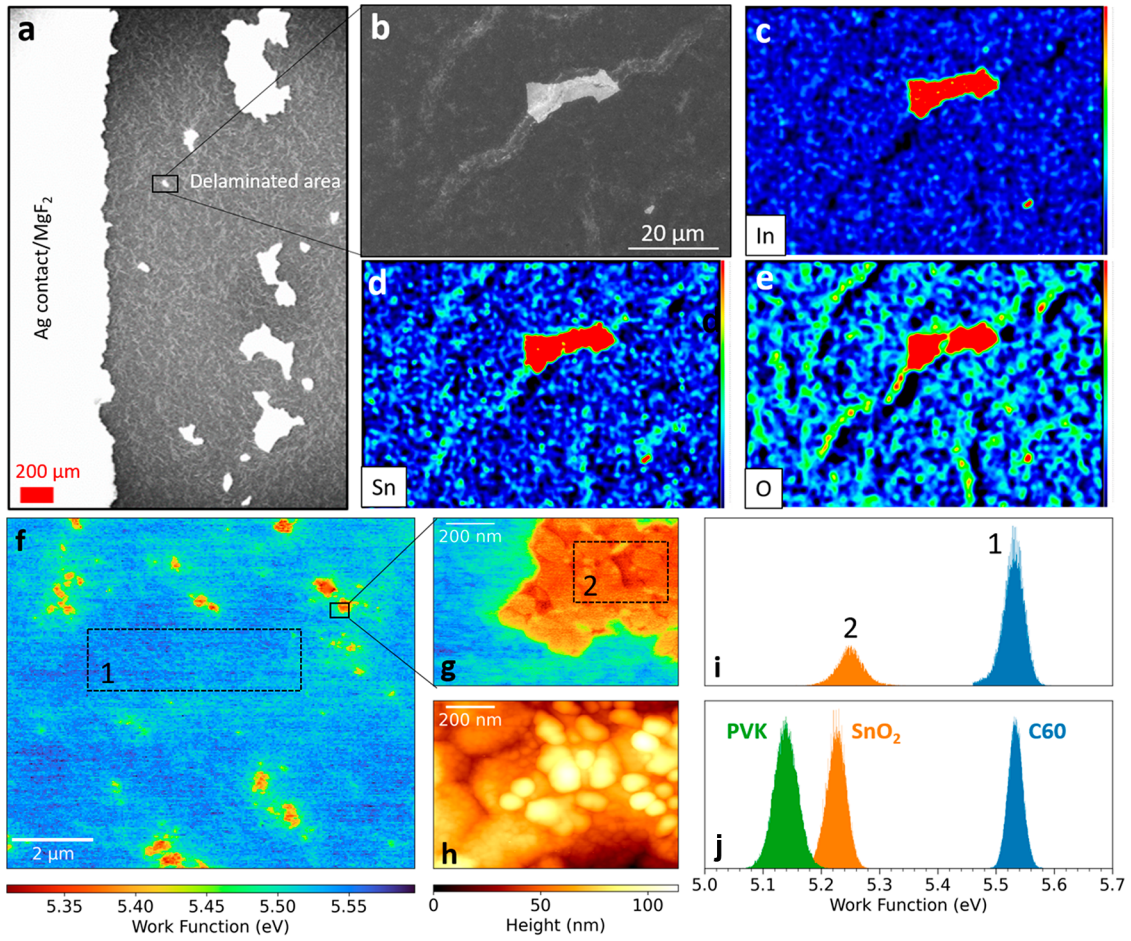

Figure 3. Microscopic investigation of the delamination. (a) Large area overview SEM image at the edge of the peeled area. (b) Closer SEM top-view image of the investigated area. (c–e) EDX mapping of indium, tin, and oxygen, respectively. (f) 10 μm^2 KPFM map of a delaminated tandem solar cell. (g, h) 1 μm^2 close-up of one of the residuals as measured by KPFM and dynamic AFM morphology, respectively. (i) Work function distributions of regions 1 (blue) and 2 (orange), corresponding to the regions delimited by dashed rectangles in f) and g). (j) Work function distributions of calibration samples consisting of Si/ITO/Perovskite (green), Si/ITO/perovskite/C_{60} (blue), and Si/ITO/perovskite/C_{60}/SnO_2 (orange).

stack, resulting in its rupture under stress.[13,14] Here, we thoroughly investigate the nature of delamination mechanism in state-of-the-art *p-i-n* tandems (Figure 1a) by intentionally peeling-off the top electrode (Figure 1b–e). We found that, the top electrode fully delaminates, even preserving the pristine conductivity of the front transparent contact (Figure S1). For improved understanding of the delamination process, we collected tilted-angle scanning electron microscopy (SEM) images at the peeling interface (Figure 1f). At the bottom of the image, the typical textured surface of the c-Si bottom cell is visibly covered by the perovskite layer. The perovskite exhibits on its surface the characteristic wrinkles induced during the crystallization process. These wrinkles are induced by the presence of Cs in the perovskite formulation and the presence of the textured substrate underneath.[17] The purple area highlights the top part of the contact (the Ag finger is covered by the MgF_2 anti-reflective coating (ARC)) that is partially lifted, while the yellow area represents the film that delaminated.

To identify the nature of the layers that delaminate, we investigated both exposed surfaces of the failed device interface, with a combination of surface sensitive (1–10 nm) X-ray and ultraviolet photoelectron spectroscopies (XPS/UPS), energy dispersive X-ray analysis (EDX), and Kelvin probe force microscopy (KPFM). Figure 2a shows the XPS survey scan of the films present on the surface emerging from the tandem (red square in the inset). The spectrum shows the typical feature of carbon in the form of fullerene (C_{60}), a single C1s peak, accompanied by characteristic shake-up satellite features,[18] with traces of elements belonging to the perovskite, but not of elements related to the contact (see Figure S2 for more details). From the quantification of the peak areas, we identified the material present on the tape (Figure 2b) as the atomic layer deposited (ALD) SnO_2 buffer layer (film composition: Sn 24 At%, O 42 At%, C 33% and a trace of I of 0.5%). To further investigate, we acquired UPS spectra of both samples with a depth sensitivity of ∼1 nm. Figure 2c shows the UPS spectrum of the surface emerging from the tandem. The secondary electron cut-off (SECO) indicates a work function (WF) of 5.15 eV, which matches well with that of pristine C_{60} measured independently on a freshly evaporated C_{60} layer as well as resulting in an acceptable ionization energy (IE) of 6.50 eV (calculated from WF + VBM − E_f). Figure 2d shows the SECO of the film present on the tape side. The energy levels are univocally attributed to SnO_2, with a deep valence band at −7.90 eV (resulting in a WF of 4.05 eV).[19,20] The UPS analysis confirms the finding of the XPS analysis, suggesting that the delamination happened on a macroscopic

https://doi.org/10.1021/acsenergylett.1c02148
ACS Energy Lett. XXXX, XXX, XXX−XXX

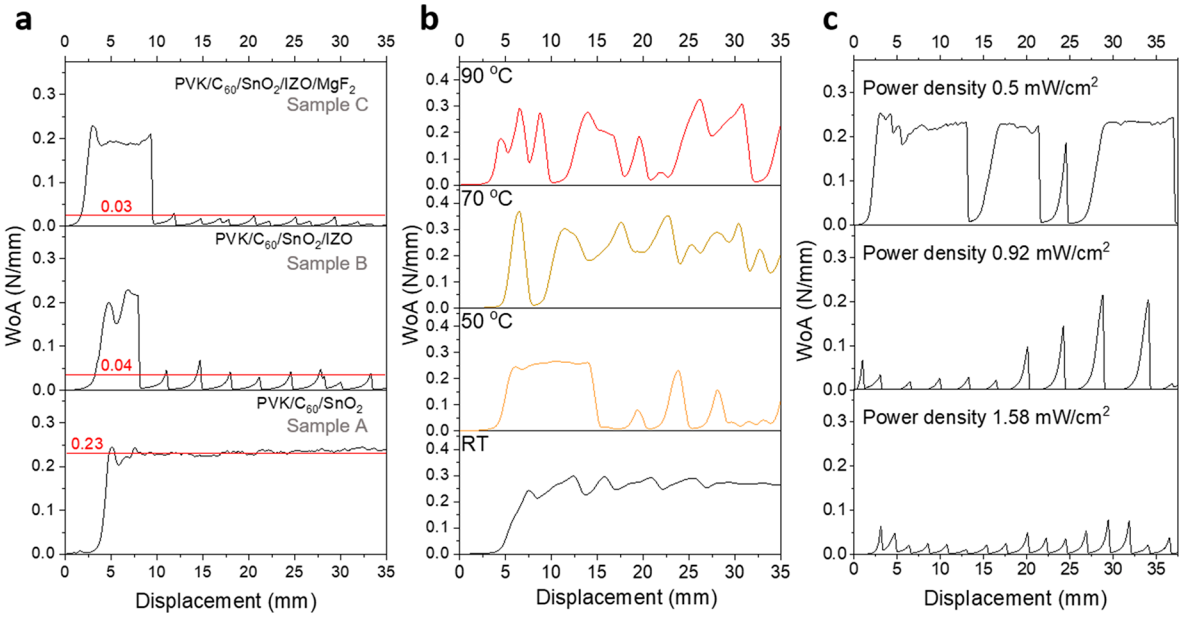

Figure 4. (a) 180-degree peel-off test for tandem test structures. PVK is the perovskite layer. Sample A (PVK/C60/SnO_2); sample B (PVK/C_{60}/SnO_2/IZO); sample C (PVK/C_{60}/SnO_2/IZO/MgF_2). The red line averages the adhesion energy in N/mm. (b) 180-degree peel-off test for three identical test structures: PVK/C_{60}/SnO_2 annealed at different temperatures: RT black, 50 °C orange, 70 °C yellow, 90 °C red. (c) Peel-off tests for tandem structures with the IZO layer deposited with different powers. The sample labeled 0.92 mW/cm^2 is the reference deposition for tandem applications.

scale at the interface between the fullerene and the SnO_2 buffer layer, as evidenced by the area bulk averaging property of the techniques.

To understand the microscopic nature of the delamination we combined EDX topography with KPFM mapping. Figure 3a shows a low-magnification SEM top view of the delaminated interface of the tandem; the white bright side represents the MgF_2 top layer, whereas the dark side is the emerging surface. With a closer look, we noticed that the delamination is not uniform. Indeed, we spotted several micrometer-sized areas where the top contact appears to be intact. Moreover, the morphology of the perovskite is not perfectly flat, and we noticed a difference in contrast on top of the wrinkles, induced by perovskite crystallization. Therefore, we performed EDX topography on one of those regions, where the top electrode overlaps on top of a wrinkle (Figure 3b). The EDX mapping of In, Sn, and O (Figure 3c–e) clearly shows that the bright area is part of the top electrode stack (which in this region consists of the ALD-SnO_2 buffer layer and indium zinc oxide (IZO) electrode) that did not delaminate with the rest of the film. Moreover, we noticed traces of Sn and O on top of the wrinkle, suggesting the presence of the SnO_2 buffer layer. This is of significant importance since the microscopic roughness of the materials can have a fundamental role in controlling the adhesion between the layers. To further investigate the microscopic nature of the delamination we took advantage of KPFM mapping in an argon ambient and in dark conditions, to avoid sample degradation during the measurement. Figure 3f shows a 10 μm^2 KPFM scan of a delaminated tandem solar cell. This map confirms the non-uniformity of the delamination at the micrometer scale, with clear presence of low WF residuals on top of a high WF substrate. Figure 3g,h shows a 1 μm^2 KPFM and morphology close-up of one of the residuals, respectively. We note the close correlation between the WF map and morphology, confirming that the micrometer-sized islands are residuals of a different chemical species than the substrate. The morphology and phase maps of the delaminated solar cell are reported in Figure S3. Figure 3i shows the distribution of the WFs measured in regions 1 (substrate) and 2 (residual), as indicated in Figure 2f and 3g by dashed rectangles. To assess the nature of the two species, we measured WF distributions of calibration samples consisting of Si/ITO/perovskite, Si/ITO/perovskite/C_{60}, and Si/ITO/perovskite/C_{60}/SnO_2 structures, shown in Figure 3l as green, blue, and orange histograms, respectively. The KPFM and morphology maps of the calibration samples are reported in Figure S3. The WF values measured by KPFM on the reference samples match well the values obtained by UPS scans on the same samples, as shown in Figure S4. A comparison with the distribution of the delaminated solar cell unequivocally shows that the exposed layer consists of a C_{60} film with SnO_2 residuals on top.

To better understand the delamination mechanism, we performed density functional theory simulations of the C_{60}/SnO_2 interface to model the adhesion between the two materials. Specifically, we studied various orientations of the C_{60} molecule on the SnO-terminated (110) surface of SnO_2. We found that the carbon atoms shared by pentagons and hexagons of the C_{60} molecule interact with both the Sn and O atoms of the SnO_2 surface with a binding energy of −0.28 eV. The optimized structure is shown in Figure S5. The Bader charge analysis demonstrated a transfer of less than 0.02 electrons from the C_{60} molecule to the SnO_2 surface. Finally, we determined that the distance between the C_{60} molecule and SnO_2 surface is 3.22 Å, falling into the physisorption range. With this information at hand, we then evaluated the fracture energy of the C_{60}/SnO_2 interface, namely the work of adhesion (WoA), using 180° peel-off measurements (Figure 4a). To isolate the fracture, we realized different test structures on top of perovskite films that mimic the tandem architecture: C_{60}/SnO_2 (sample A), C_{60}/SnO_2/IZO (sample B), and C_{60}/SnO_2/IZO/MgF_2 (sample C). Surprisingly, we found that the WoA

https://doi.org/10.1021/acsenergylett.1c02148
ACS Energy Lett. XXXX, XXX, XXX−XXX

between the C_{60} and the SnO_2 bilayer (~0.23 N/mm) is higher than that of the peeling tape interface (~0.20 N/mm, see Figure S6). Indeed, we did not notice any delamination on sample A. However, when the SnO_2 is capped with a sputtered IZO layer as transparent electrode (sample B) we experienced the same delamination behavior of the tandem itself, fracturing at the C_{60}/SnO_2 interface. Moreover, we noticed that the delamination happens via a slip-and-stick mechanism and, as expected, is accentuated in the presence of film edges (see Figure S7). From the delamination profile of sample B we evaluated a WoA of 0.04 N/mm. Next, we found that coating the IZO layer with an additional ARC layer of MgF_2 (sample C) further reduces the WoA of the C_{60}/SnO_2 interface (0.03 N/mm). The MgF_2 layer is adopted at the single-cell level to enhance the current response; it is not meant to be included at the module level, since the encapsulant features a similarly low refractive index. However, at the lab level and for practical purposes, tandem devices are often laminated with MgF_2 either for stability or outdoor performance evaluation.[4,21] In our case, we found that the presence of MgF_2 as second ARC is deteriorating the long-term stability of the device, as it enhances the possibility of delamination. However, the lower adhesion energy attributed to the presence of IZO or MgF_2 is not due to the layers themselves, but rather to a weakening of the C_{60}/SnO_2 interface during the IZO sputtering or MgF_2 thermal evaporation processes. Indeed, it is likely that during these depositions the sample heats up, particularly during the MgF_2 deposition (reaching temperature close to ~50 °C). The higher temperature weakens the bonding between C_{60} and SnO_2, favoring the delamination process. Therefore, to validate our hypothesis, we performed a second peel-off experiment (Figure 4b) with four identical test-structures of perovskite/C_{60}/SnO_2 but annealed at different temperatures (room temperature (RT) gray line, 50 °C orange line, 70 °C yellow line, and 90 °C red line). The outcome of the experiment validated our hypothesis. Indeed, the sample without annealing (RT) showed a pattern similar to sample A in Figure 4a in terms of profile and peeling force. On the contrary, a mild annealing at 50 °C (and consistently at higher temperatures) showed the clear features of delamination, as evidenced by the pictures of the samples in Figure S8. Lastly, we shifted our attention to the impact of the IZO deposition. The direct deposition of TCOs by radio frequency (rf) sputtering is known to possible create damage in the underlying layers.[22] Even in silicon heterojunction solar cell manufacturing the TCO deposition is followed by an annealing step to recover the damage done to the amorphous silicon contact layers during such sputtering. In perovskite/silicon tandems, the SnO_2 buffer layer protects the soft fullerene and perovskite layers from the deposition of IZO. Figure 4a shows a clear difference between sample A and B, suggesting that the IZO deposition affects the WoA. Therefore, we deposited IZO layers with different power densities: 0.5, 0.92, and 1.58 mW/cm^2, which represent soft deposition, our baseline deposition, and a faster deposition conditions, respectively (all the films share the same IZO thickness). Figure 4c shows the WoA profiles for the three samples. We noted that there is a correlation between the deposition power and the interfacial mechanical properties. Indeed, at higher power the samples delaminate easier, showing a lower WoA. To validate our findings, we performed a statistical analysis over a batch of six samples. Then we determined the average energy per sample by integrating the WoA (Figure S9). The distribution clearly shows that the deposition of the IZO plays a key role in the delamination and suggests that a precise control of the deposition conditions is strategic to prevent this issue.

Few works in the past addressed delamination in PSCs. Cheacharoen et al., investigated this problem at the single-junction level and proposed the fracture of the PCBM layer, a functionalized version of C_{60}, as the origin.[13,14] Here we propose that the delamination originates at the C_{60}/SnO_2 interface with a neat separation of the two films at the macroscopic level, but influenced by the perovskite roughness at the microscopic level. Yet, in both cases, it is clear that the presence of the fullerene (or its derivatives) poses a serious roadblock toward the development of mechanically stable perovskite-based solar cells. Indeed, the challenge is not limited to the fabrication of modules, but also to the stability of the performances. In real applications, the temperature of the tandems can reach up to 50−60 °C at the peak-sun hours.[1,23] The periodic temperature changes typical for outdoor performance impose cyclic stresses to the materials, in particular to those that have different thermal expansion coefficients. Therefore, it is of high urgency to address the delamination issue at the widely used C_{60} interface within the perovskite community.

Fullerene-based n-type contacts are an iconic part of *p-i-n* PSCs,[24] in particular thanks to their unique property in reducing the hysteresis in the current−voltage characteristic.[25,26] Currently, there are no reasonable candidates that can be used in this polarity configuration as an alternative to fullerenes without losing performance, stability, or exacerbating hysteresis.[27] Therefore, the best approach for p-i-n PSCs to address delamination is the functionalization of the fullerene and its surface.[28] In this direction, in tandems, particular attention should be given toward the realization of a strong chemical bond between the C_{60} and the buffer layer (inserted between C_{60} layer and sputtered transparent top electrode), to enable a proper lamination of stable perovskite/silicon tandems. This bond can be enhanced either with an *in situ* approach or with other layers deposited on top of the fullerene. In both cases, the treatment must respect the perovskite constrains, in terms of solvent compatibility and temperature processing. In parallel, particular attention should be given to preserve the electronic properties of the ETL and to avoid parasitic absorption that can affect the current output of the tandem. Lastly, we proved that the processing conditions for the tandem fabrication have a significant role in delamination. Temperature treatments or post-annealing treatments negatively affect the weak adhesion between C_{60} and SnO_2 and they should be minimized or avoided completely. Moreover, the impact of the sputtering process should be reduced for example employing soft-landing depositions such as the hollow cathode technique and the parallel sputtering configuration.

In this work, we showed the origin of the delamination in perovskite/silicon tandem solar cells. Delamination is among the most serious concerns for the manufacturing of tandem modules and for the stability of the tandem performances, yet hardly discussed to date. Contrarily to what has been reported earlier for single-junction PSCs, we found that delamination happens at the interface between the C_{60} extraction layer and the SnO_2 buffer layer. Moreover, we realized that the adhesion between the two layers is influenced by the perovskite morphology; indeed, the wrinkles induced during the perovskite crystallization retain microscopically the adhesion between the C_{60} and SnO_2. This provides the opportunity in

https://doi.org/10.1021/acsenergylett.1c02148
ACS Energy Lett. XXXX, XXX, XXX−XXX

the near future to engineer the roughness of the perovskite layer in such a way that the probability for delamination to occur is reduced. Furthermore, we showed that the temperature during the processing of the tandem has an influence on the adhesion between the C_{60} and SnO_2. Such an understanding is pivotal to improve the tandem fabrication, toward more stable performances.

■ ASSOCIATED CONTENT

Supporting Information

The Supporting Information is available free of charge at https://pubs.acs.org/doi/10.1021/acsenergylett.1c02148.

Experimental section; peeling of the top electrode; XPS spectra after the peeling of the electrode; morphology and KPFM maps; work function comparison; DFT calculations; work of adhesion calibration and stick-and-slip behavior; effect of temperature on the delamination; statistic distribution of the work of adhesion as a function of the IZO sputtering power (PDF)

Video showing the 180° stick-and-slip behavior (MP4)

■ AUTHOR INFORMATION

Corresponding Authors

Michele De Bastiani − *KAUST Solar Center (KSC), Physical Sciences and Engineering Division (PSE), King Abdullah University of Science and Technology (KAUST), Thuwal 23955-6900, Kingdom of Saudi Arabia;* orcid.org/0000-0002-4870-2699; Email: michele.debastiani@kaust.edu.sa

Stefaan De Wolf − *KAUST Solar Center (KSC), Physical Sciences and Engineering Division (PSE), King Abdullah University of Science and Technology (KAUST), Thuwal 23955-6900, Kingdom of Saudi Arabia;* orcid.org/0000-0003-1619-9061; Email: stefaan.dewolf@kaust.edu.sa

Authors

Giovanni Armaroli − *Department of Physics and Astronomy, University of Bologna, 40127 Bologna, Italy*

Rawan Jalmood − *KAUST Solar Center (KSC), Physical Sciences and Engineering Division (PSE), King Abdullah University of Science and Technology (KAUST), Thuwal 23955-6900, Kingdom of Saudi Arabia*

Laura Ferlauto − *Department of Physics and Astronomy, University of Bologna, 40127 Bologna, Italy; Interdepartmental Center for Industrial Research of the University of Bologna (CIRI-MAM), 40136 Bologna, Italy;* orcid.org/0000-0003-2131-6795

Xiaole Li − *King Abdullah University of Science and Technology (KAUST), Physical Science and Engineering Division, Mechanics of Composites for Energy and Mobility Lab., Thuwal 23955-6900, Saudi Arabia*

Ran Tao − *King Abdullah University of Science and Technology (KAUST), Physical Science and Engineering Division, Mechanics of Composites for Energy and Mobility Lab., Thuwal 23955-6900, Saudi Arabia*

George T. Harrison − *KAUST Solar Center (KSC), Physical Sciences and Engineering Division (PSE), King Abdullah University of Science and Technology (KAUST), Thuwal 23955-6900, Kingdom of Saudi Arabia*

Mathan K. Eswaran − *KAUST Solar Center (KSC), Physical Sciences and Engineering Division (PSE), King Abdullah University of Science and Technology (KAUST), Thuwal 23955-6900, Kingdom of Saudi Arabia*

Randi Azmi − *KAUST Solar Center (KSC), Physical Sciences and Engineering Division (PSE), King Abdullah University of Science and Technology (KAUST), Thuwal 23955-6900, Kingdom of Saudi Arabia*

Maxime Babics − *KAUST Solar Center (KSC), Physical Sciences and Engineering Division (PSE), King Abdullah University of Science and Technology (KAUST), Thuwal 23955-6900, Kingdom of Saudi Arabia*

Anand S. Subbiah − *KAUST Solar Center (KSC), Physical Sciences and Engineering Division (PSE), King Abdullah University of Science and Technology (KAUST), Thuwal 23955-6900, Kingdom of Saudi Arabia;* orcid.org/0000-0002-7505-3209

Erkan Aydin − *KAUST Solar Center (KSC), Physical Sciences and Engineering Division (PSE), King Abdullah University of Science and Technology (KAUST), Thuwal 23955-6900, Kingdom of Saudi Arabia;* orcid.org/0000-0002-8849-2788

Thomas G. Allen − *KAUST Solar Center (KSC), Physical Sciences and Engineering Division (PSE), King Abdullah University of Science and Technology (KAUST), Thuwal 23955-6900, Kingdom of Saudi Arabia*

Craig Combe − *KAUST Solar Center (KSC), Physical Sciences and Engineering Division (PSE), King Abdullah University of Science and Technology (KAUST), Thuwal 23955-6900, Kingdom of Saudi Arabia*

Tobias Cramer − *Department of Physics and Astronomy, University of Bologna, 40127 Bologna, Italy;* orcid.org/0000-0002-5993-3388

Derya Baran − *KAUST Solar Center (KSC), Physical Sciences and Engineering Division (PSE), King Abdullah University of Science and Technology (KAUST), Thuwal 23955-6900, Kingdom of Saudi Arabia;* orcid.org/0000-0003-2196-8187

Udo Schwingenschlögl − *KAUST Solar Center (KSC), Physical Sciences and Engineering Division (PSE), King Abdullah University of Science and Technology (KAUST), Thuwal 23955-6900, Kingdom of Saudi Arabia;* orcid.org/0000-0003-4179-7231

Gilles Lubineau − *King Abdullah University of Science and Technology (KAUST), Physical Science and Engineering Division, Mechanics of Composites for Energy and Mobility Lab., Thuwal 23955-6900, Saudi Arabia;* orcid.org/0000-0002-7370-6093

Daniela Cavalcoli − *Department of Physics and Astronomy, University of Bologna, 40127 Bologna, Italy;* orcid.org/0000-0002-2417-1248

Complete contact information is available at: https://pubs.acs.org/10.1021/acsenergylett.1c02148

Notes

The authors declare no competing financial interest.

■ ACKNOWLEDGMENTS

This work was supported by the King Abdullah University of Science and Technology (KAUST) Office of Sponsored Research (OSR) under award nos. KAUST OSR-2018-CARF/CCF-3079, KAUST OSR-CRG RF/1/3383, KAUST OSR-CRG2018-3737, and IED OSR-2019-4208. L.F. and D.C. acknowledge funding from the European Community through the POR-FESR "FORTRESS" project, grant no. I38D18000150009 (PG/2018/629121).

REFERENCES

(1) Aydin, E.; et al. Interplay between temperature and bandgap energies on the outdoor performance of perovskite/silicon tandem solar cells. *Nature Energy* **2020**, *5*, 851−859.

(2) Al-Ashouri, A.; et al. Monolithic perovskite/silicon tandem solar cell with> 29% efficiency by enhanced hole extraction. *Science* **2020**, *370*, 1300−1309.

(3) Köhnen, E.; et al. 27.9% Efficient Monolithic Perovskite/Silicon Tandem Solar Cells on Industry Compatible Bottom Cells. *Solar RRL* **2021**, *5*, 2100244.

(4) De Bastiani, M.; et al. Efficient bifacial monolithic perovskite/silicon tandem solar cells via bandgap engineering. *Nature Energy* **2021**, *6*, 167.

(5) Isikgor, F. H.; et al. Concurrent cationic and anionic perovskite defect passivation enables 27.4% perovskite/silicon tandems with suppression of halide segregation. *Joule* **2021**, *5*, 1566−1586.

(6) Aydin, E.; et al. Ligand-bridged charge extraction and enhanced quantum efficiency enable efficient n−i−p perovskite/silicon tandem solar cells. *Energy Environ. Sci.* **2021**, *14*, 4377.

(7) Hou, Y.; et al. Efficient tandem solar cells with solution-processed perovskite on textured crystalline silicon. *Science* **2020**, *367*, 1135−1140.

(8) Xu, J.; et al. Triple-halide wide−band gap perovskites with suppressed phase segregation for efficient tandems. *Science* **2020**, *367*, 1097−1104.

(9) Kim, D.; et al. Efficient, stable silicon tandem cells enabled by anion-engineered wide-bandgap perovskites. *Science* **2020**, *368*, 155−160.

(10) De Bastiani, M.; et al. All Set for Efficient and Reliable Perovskite/Silicon Tandem Photovoltaic Modules? *Solar RRL* **2021**, *5*, 2100493.

(11) Kopecek, R.; Libal, J. Bifacial Photovoltaics 2021: Status, Opportunities and Challenges. *Energies* **2021**, *14*, 2076.

(12) Ugur, E.; et al. How Humidity and Light Exposure Change the Photophysics of Metal Halide Perovskite Solar Cells. *Solar RRL* **2020**, *4*, 2000382.

(13) Cheacharoen, R.; et al. Encapsulating perovskite solar cells to withstand damp heat and thermal cycling. *Sustainable Energy & Fuels* **2018**, *2*, 2398−2406.

(14) Cheacharoen, R.; et al. Design and understanding of encapsulated perovskite solar cells to withstand temperature cycling. *Energy Environ. Sci.* **2018**, *11*, 144−150.

(15) Shi, L.; et al. Gas chromatography−mass spectrometry analyses of encapsulated stable perovskite solar cells. *Science* **2020**, *368* (6497), aba2412.

(16) Rolston, N.; et al. Mechanical integrity of solution-processed perovskite solar cells. *Extreme Mechanics Letters* **2016**, *9*, 353−358.

(17) Bush, K. A.; et al. Controlling thin-film stress and wrinkling during perovskite film formation. *ACS Energy Letters* **2018**, *3*, 1225−1232.

(18) Liu, H.; Taheri, B.; Jia, W. Anomalous optical response of C 60 and C 70 in toluene. *Phys. Rev. B* **1994**, *49*, 10166.

(19) Kuang, Y.; et al. Low-temperature plasma-assisted atomic-layer-deposited SnO2 as an electron transport layer in planar Perovskite solar cells. *ACS Appl. Mater. Interfaces* **2018**, *10*, 30367−30378.

(20) Dong, Q.; et al. Interpenetrating interfaces for efficient perovskite solar cells with high operational stability and mechanical robustness. *Nat. Commun.* **2021**, *12*, 6484.

(21) De Bastiani, M.; et al. Toward Stable Monolithic Perovskite/Silicon Tandem Photovoltaics: A Six-Month Outdoor Performance Study in a Hot and Humid Climate. *ACS Energy Lett.* **2021**, *6*, 2944−2951.

(22) Aydin, E.; et al. Sputtered transparent electrodes for optoelectronic devices: Induced damage and mitigation strategies. *Matter* **2021**, *4*, 3549−3584.

(23) Tress, W.; et al. Performance of perovskite solar cells under simulated temperature-illumination real-world operating conditions. *Nature energy* **2019**, *4*, 568−574.

(24) Docampo, P.; Ball, J. M.; Darwich, M.; Eperon, G. E.; Snaith, H. J. Efficient organometal trihalide perovskite planar-heterojunction solar cells on flexible polymer substrates. *Nat. Commun.* **2013**, *4*, 2761.

(25) Shao, Y.; Xiao, Z.; Bi, C.; Yuan, Y.; Huang, J. Origin and elimination of photocurrent hysteresis by fullerene passivation in CH 3 NH 3 PbI 3 planar heterojunction solar cells. *Nat. Commun.* **2014**, *5*, 5784.

(26) De Bastiani, M.; et al. Ion migration and the role of preconditioning cycles in the stabilization of the J−V characteristics of inverted hybrid perovskite solar cells. *Adv. Energy Mater.* **2016**, *6*, 1501453.

(27) Kim, S. S.; Bae, S.; Jo, W. H. A perylene diimide-based non-fullerene acceptor as an electron transporting material for inverted perovskite solar cells. *RSC Adv.* **2016**, *6*, 19923−19927.

(28) Olah, G. A.; Bucsi, I.; Aniszfeld, R.; Prakash, G. S. Chemical reactivity and functionalization of C60 and C70 fullerenes. *Carbon* **1992**, *30*, 1203−1211.

https://doi.org/10.1021/acsenergylett.1c02148
ACS Energy Lett. XXXX, XXX, XXX−XXX